Phys. Med. Biol. **45** (2000) 1477–1494. Printed in the UK PII: S0031-9155(00)07821-0

Three-dimensional sonoelastography: principles and practices

L S Taylor†, B C Porter†, D J Rubens‡ and K J Parker†

† Department of Electrical and Computer Engineering, Strong Memorial Hospital, University of Rochester, Rochester, NY 14627, USA
‡ Department of Radiology, Strong Memorial Hospital, University of Rochester, Rochester, NY 14627, USA

E-mail: parker@seas.rochester.edu

Received 14 September 1999

Abstract. Sonoelastography is an ultrasound imaging technique where low-amplitude, low-frequency shear waves (less than 0.1 mm displacement and less than 1 kHz frequency) are propagated through internal organs, while real-time Doppler techniques are used to image the resulting vibration pattern. When a discrete hard inhomogeneity, such as a tumour, is present within a region of soft tissue, a decrease in the vibration amplitude will occur at its location. This forms the basis for tumour detection using sonoelastography. For three-dimensional (3D) imaging the acquisition of sequential tomographic slices using this technique, combined with image segmentation, enables the reconstruction, quantification and visualization of tumour volumes. Sonoelastography and magnetic resonance images (MRI) of a tissue phantom containing a hard isoechoic inclusion are compared to evaluate the accuracy of this method. The tumour delineation from sonoelastography was found to have good agreement with the tumour from MRI except for a bleeding at one of its ends. Although sonoelastography is still in an experimental phase, the principles behind this imaging modality are explained and some practical aspects of acquiring sonoelastography images are described. Results from a 3D sonoelastography reconstruction of a tissue mimicking phantom and an *ex vivo* whole prostate specimen are presented.

1. Introduction

Many forms of cancer are manifest as hard lesions in soft tissue, and because of this physicians use palpation to detect the presence of hard tumours within the human body (Carvalhal *et al* 1999, Obek *et al* 1999). The American Cancer Society encourages all women over 20 years of age to perform a regular breast self-examination to detect lumps and other abnormalities. Digital rectal examination of the prostate is routinely performed on men who have reached middle age to screen for cancer. Unfortunately palpation is usually limited to the detection of lesions near the tissue surface and to lesions with high stiffness contrast. Two widely used medical imaging modalities, magnetic resonance imaging (MRI) and ultrasound (US), have reported accuracy levels for detecting prostate cancer that miss a significant portion of the cancerous lesions. For example, Ellis *et al* (1994) in a study of patients known to have prostate cancer imaged 320 patients using MRI and 343 patients using US. They reported that about one-third of cancers were missed by each modality. Melchior and Brawer (1996) reported on their experience with 2231 ultrasound-guided prostate biopsies and found that failure to biopsy isoechoic sectors would have resulting in missing 20% of the men with prostate cancer. It is plausible therefore, that an imaging modality that would reliably detect hard tumours in soft tissue would be a beneficial supplement to the existing techniques.

0031-9155/00/061477+18$30.00

Because of this there has been ongoing interest in both estimating the elastic properties of tissue and in imaging hard tumours. Gao *et al* (1996) did a comprehensive review of the literature on techniques for accomplishing this objective. In the area of ultrasonic imaging, techniques for elasticity imaging might currently be broken down into three methods:

- compression elastography or strain imaging
- transient elastography
- vibration sonoelastography.

Vibration sonoelastography is the subject of this paper. A representative example of the strain imaging group is found in Ophir *et al* (1991) where a method for elasticity imaging, referred to by those authors as elastography, is described. Compression is applied to a tissue sample, then pre-compression and post compression echo return signals are compared, using correlation techniques to calculate the strain map in the tissue. A paper by O'Donnell *et al* (1994) provides another strain imaging example. A recent paper by Catheline *et al* (1999) describes the transient elastography technique. This method uses a low-frequency transient vibration to create displacements in tissue, which are then detected using pulse-echo ultrasound. The numerical values of elasticity and viscosity are deduced from the wave propagation observed before the echoes from the tissue boundaries contaminate the data. Relative stiffness imaging (slowness or inverse velocity image) of a region of interest with two different elasticities was produced using this method. An earlier technique, vibration sonoelastography, is the subject of this paper.

Sonoelastography imaging uses real-time ultrasound Doppler techniques to image the vibration pattern resulting from the propagation of low-frequency (less than 1 kHz) shear waves that are propagated through deep tissue. The low-frequency vibration is provided by an external source, such as an audio speaker or a piston shaker, which is brought into close contact with the patient or tissue sample. The shear source is then driven by signals in the audio frequency range. When a region of uniform tissue contains a hard lesion there is a local decrease in the peak vibration amplitude at the lesion. Doppler techniques are used to estimate the vibration amplitude and phase within a region of interest. In vibration amplitude sonoelastography we map these amplitude estimates to a grey scale where high vibration is bright and lower vibrations are dark. Early references include Krouskop *et al* (1987), Lerner *et al* (1988) and Yamakoshi *et al* (1990).

The work described in the paper by Krouskop *et al* resembles what we are calling sonoelastography in that they employed forced vibration to induce motions in tissue, and used ultrasound to detect that motion. Their objective was to make non-invasive measurements of the elastic modulus of the tissue. They did not apply their method to imaging. Yamakoshi *et al* developed a similar approach, mapping both amplitude and phase of the vibration using a Doppler signal detection technique. Although they observed that an inhomogeneity will cause a localized disturbance in the vibration phase image, their main objective was measuring the wave propagation velocity, from which the shear modulus can be calculated. Lerner *et al* were the first to propose vibration amplitude imaging using ultrasound and forced low-frequency vibration. The current paper represents a refinement of the techniques proposed in that paper.

In this paper we present the relevant principles and current practices for sonoelastography. The next section on theory and methods (section 2) reviews aspects of elastodynamic theory that allow imaging of the relative elasticity of tissue. Section 2.1 discusses the conditions under which the vibration field in a region of tissue correlates with the underlying tissue elasticity. In section 2.2 the signal processing that enables the vibration field in a region of tissue to be imaged using Doppler spectral ultrasound techniques is described. Details and results of a computer simulation performed to study the relationship between vibration

amplitude and Doppler variance are presented. Modal patterns in the vibration field have been a major source of artefacts when imaging phantoms. The theory section concludes with an analysis of vibration modal patterns. The methods section then follows with a description of the experimental protocols used for imaging and image processing methods, then describes the phantom and *ex vivo* tissue specimens used. Section 3 presents images from phantom and *ex vivo* tissue experiments. The paper closes with a discussion and conclusion (section 4).

2. Theory and methods

2.1. Elasticity theory

The theory of vibration sonoelastography is based on the propagation of shear waves through elastic biomaterials. The general problem of vibration propagation within a complex organ such as the kidney is difficult to pose analytically, given the inhomogeneous tissue, the complex shape and variable boundary conditions. Nonetheless, some generalizations can be made, and some simplified solutions obtained, for the important case of a hard, focal lesion within softer tissue parenchyma. Gao *et al* (1995) formulated mathematical models for simplified cases. This work has been extended to quantify the problem of the detectability of a hard, but otherwise isoechoic, tumour in softer tissue (Parker *et al* 1998). In these treatments, the lesion is modelled as an elastic inhomogeneity within a larger, lossy homogeneous and isotropic elastic medium. The homogeneous medium has an elastic modulus E_0, whereas the small lesion has a stiffness of $E_0 + \Delta E$. The shear wave equation can be solved by analytical or finite element techniques, to predict the resulting vibration pattern within the tissue. The general trends are that a small stiff lesion will appear as a local void or deficit of the vibration pattern. The apparent vibration amplitude contrast (the per cent decrease in vibration amplitude within the lesion compared with the otherwise homogeneous tissue) increases with increasing frequency, increasing stiffness and increasing size of the lesion. However, in real tissue the increasing losses with increasing frequency place a practical upper limit on the vibration frequency that can be applied. Our results show that a 4 mm tumour that is seven times the elastic stiffness of the surrounding tissue will produce a 40% decrease in vibration at 400 Hz. However, in organs with very regular shapes, the role of modal patterns (standing waves) can complicate the interpretation of the images.

2.2. Signal processing

2.2.1. Vibration estimation from the power spectrum. In this section we describe the theoretical work that established the relationship between the power spectrum of a vibrating object and the power spectrum of its backscattered ultrasound signal. Early in the 1990s it was shown that the vibration amplitude of a scatterer in sinusoidal motion alters the power spectrum of an insonifying ultrasound beam in a predictable manner. Huang *et al* (1990) determined that when the frequency of vibration is much smaller than the ultrasound frequency the scatterer angle modulates the power spectrum of the ultrasound. It was shown for continuous wave ultrasound that the spectrum of a vibrating target has discrete spectral lines weighted by Bessel functions of the first kind and a simple relationship between the spread (standard deviation) of the Doppler spectrum and the vibration amplitude was derived. First the modulation index, β, of the signal was shown to be directly related to the vibration amplitude of the scatterer by the following relationship:

$$\beta = \frac{2\varepsilon_m \omega}{c} \tag{1}$$

where ε_m is the vibration amplitude, ω is the radian frequency of the ultrasound wave and c is the speed of sound through the medium. This relation shows that the estimation of the vibration amplitude is equivalent to estimating the modulation coefficient. Huang *et al* went on further to derive an equation to estimate the modulation coefficient from the standard deviation of the power spectrum:

$$\beta = \frac{\sqrt{2}\sigma}{\omega_v} \tag{2}$$

where ω_v is the vibration frequency. Combining equations (1) and (2) the following relation is obtained:

$$\sigma = \frac{\sqrt{2}\varepsilon_m \omega \omega_v}{c}. \tag{3}$$

This linear relationship between vibration amplitude and the standard deviation of the power spectrum forms the basis for vibration amplitude imaging.

2.2.2. Estimating spectral spread. In this section we describe how the vibration field in a region of tissue can be imaged using Doppler techniques. Modern ultrasound scanners that incorporate colour flow Doppler imaging usually accomplish this task using real-time autocorrelation estimators (Kasai *et al* 1985, Jensen 1996) that return the mean frequency and variance of the power spectrum. In conventional flow imaging the mean frequency is used to estimate the mean velocity. In vibration imaging forced sinusoidal motion causes the tissue displacement to oscillate around its rest position so linear mean velocity does not provide any information about vibration amplitude. However, since variance is the square of standard deviation the relationship between vibration amplitude and variance will be parabolic. To create a sonoelastography image of the vibration field the real-time variance estimate for each pixel is mapped to the screen as a grey scale.

The experiments described in this paper were made using a General Electric Logiq 700 ultrasound scanner modified to display the variance estimate described above. The vibration estimator used in this machine estimates the variance using a normalized autocorrelation function. A set of 8 to 16 samples is acquired from successive A-lines. Because the variance estimator uses normalized autocorrelation, the images have a low susceptibility to the speckle pattern or echogenicity variations in B-scan images. That is, relative echogenicity of targets will not influence the vibration estimation over a wide dynamic range.

In order to understand the specific imaging parameters for the system and the impact of using a pulsed Doppler system a computer simulation was performed to study the relationship between vibration amplitude and variance. The vibration estimator used in these experiments estimates the variance using the following relation:

$$\sigma^2 = \frac{2}{T_{prf}^2}\left(1 - \frac{|R(T_{prf})|}{R(0)}\right) \tag{4}$$

where T_{prf} is the time interval at which ultrasonic pulses are emitted and $R(\ )$ is the autocorrelation function of the signal and σ^2 its variance. $R(0)$ is the autocorrelation function at zero lag, $R(T_{prf})$ is the autocorrelation function evaluated at a lag of T_{prf}, the time between successive ultrasound pulses. Derivation of this equation is given in Kasai *et al* (1985). If we recall that $R(0)$ is the energy of the signal we can see that the variance estimate is normalized for $R(0)$ and hence is not sensitive to the amplitude of the signal when using equation (4). The variance estimate will have a low susceptibility to echogenicity variations because of this normalization.

A well known property of the autocorrelation function is that it is always maximum when evaluated at zero lag. The ratio in (4) is always less than 1 so the maximum value of σ^2, the variance, is equal to

$$\mathrm{Max}(\sigma^2) = \frac{2}{T_{prf}^2}. \tag{5}$$

To study the effect of how variance changes as vibration amplitude is varied using equation (4) we need a representation of the backscatter of a series of Doppler ultrasound pulses from a scatterer in harmonic motion. We modelled a single ultrasound pulse as $p(t) = g(t)\cos 2\pi f_c t$, where $g(t)$ is a Gaussian envelope centred at time $t = 0$, with a standard deviation of 173 ns and $f_c = 5$ MHz. The scatterer was modelled as being located at a distance d_0 from the ultrasound transducer moving sinusoidally around its centre position with a peak vibration amplitude of ε_m. Its distance d from the transducer varies with time according to the equation $d = d_0 - \varepsilon_m \sin 2\pi f_v t$, where $f_v = 200$ Hz, the frequency of vibration. Travelling at the speed of sound c, the round-trip time from the transducer to the scatterer and back can be calculated from the equation $t_d = 2d/c = 2(d_0 - \varepsilon_m \sin 2\pi f_v t)/c$. The backscatter from a single pulse will be: $e(t) = Ap(t - 2(d_0 - \varepsilon_m \sin 2\pi f_v t)/c)$, where A is the amplitude of the backscatter including echogenicity, the scattering coefficient and attenuation effects.

A sequence of 16 pulses, $p(t)$, was used to simulate a colour flow packet, where the first pulse is emitted at time $t = 0$ and each successive pulse is emitted $T_{prf} = 1$ ms after the preceding one. To simulate the quadrature demodulation used to process colour flow packets for Doppler estimates, we used the approach given in chapter 6 of Jensen (1996). For the I channel we sampled the returning 16 pulses (i.e. $e(t)$ received at 1 ms intervals) at the times $t = n\ T_{prf} + 2d_0/c$, $n = 1, 2, \ldots,16$ and the Q channel by sampling at the times $t = n\ T_{prf} + 2d_0/c + 1/(4f_c)$, $n = 1, 2, \ldots,16$. Note that the Q channel is sampled one-quarter of a cycle after the I channel. Representing the samples from the I and Q channels by $I(n)$ and $Q(n)$ respectively, the sampled backscattered demodulated signal is $s(n) = I(n) + \mathrm{j}Q(n)$, where $\mathrm{j} = \sqrt{-1}$ and $n = 1, 2, \ldots,16$. The required autocorrelations for use in equation (4) are then calculated from the equations:

$$R(0) = \sum s(n)s^*(n) \qquad \text{summation is over } n = 1, 2, \ldots 15 \tag{6}$$

$$R(T_{prf}) = \sum s(n+1)s^*(n) \qquad \text{summation is over } n = 1, 2, \ldots 15 \tag{7}$$

where the * denotes complex conjugation. The value of the peak vibration amplitude, ε_m, was varied from 0 to 120 μm and σ^2 was calculated for each by using equations (6) and (7) in equation (4). In this way the curves of figures 1 and 2 were produced.

Figure 1(*a*) shows the relationship between vibration amplitude and the variance estimate for an imaging sequence using a centre frequency of 5 MHz and a vibration frequency of 200 Hz as determined by the computer simulation described above. The curve is parabolic in shape until the 100 μm vibration level where aliasing causes the curve to bend down. In all the images of figure 1 we have normalized the results of the variance estimates at different vibration amplitudes using equation (5) to the maximum estimate of variance possible at that pulse repetition frequency. The abscissa is normalized for the maximum value attainable before aliasing.

During conventional colour flow imaging a wall filter provides the useful function of eliminating the d.c. component of the echo signal, suppressing the otherwise strong signal from stationary specular tissue such as the walls of the blood vessels. Since sonoelastography estimates the vibration amplitude of the tissue from the variance of the power spectral density of the return signal, use of a conventional wall filter has the deleterious effect of destroying the smooth parabolic relationship between vibration amplitude and grey-scale value. This occurs

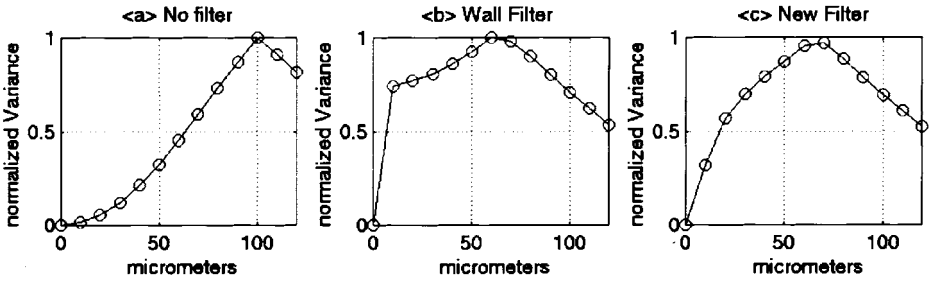

(*a*) (*b*) (*c*)

Figure 1. Plots of the vibration response of the variance estimator used for sonoelastography imaging from a computer simulation with a 5 MHz pulsed Doppler ultrasound, PRF 1000 Hz and an applied vibration of 200 Hz. The normalized variance (i.e. estimated value divided by the maximum value allowed by the estimator) is plotted versus the peak vibration amplitude. (*a*) Vibration estimator response with no filter. The curve is a parabola with an intercept at the origin. The curve is monotonic until the peak variance is reached. At higher vibration levels aliasing makes the curve decrease. (*b*) Vibration estimator response with a conventional wall filter. The response rises rapidly to a high grey-scale level producing near binary images. (*c*) Vibration estimator response with a sensitivity-enhancing filter. Comparing variance estimates for equivalent vibration amplitudes in (*a*) will verify that vibration sensitivity has been enhanced.

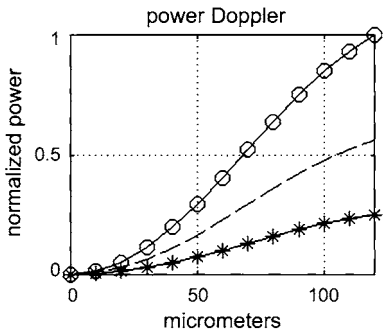

Figure 2. Plot of computer simulation of the vibration response of a power Doppler system. System parameters are the same as in figure 1. A family of curves is shown because the response depends on the signal strength from the pixel. The plot with circles indicates a unit response, the one with dashed lines has a signal strength of $3/4$ and the curve with asterisks has a strength of $1/2$. Power Doppler is not an effective vibration estimator because each estimate is biased by the echo strength from the region of tissue being imaged.

because echo signals from the lowest vibration amplitudes have a significant fraction of their power in the zero or carrier frequency. Suppression of the carrier causes an overestimate of the variance at low amplitudes so the images tend towards being binary with dark corresponding to a very low vibration and bright corresponding to a high vibration. Figure 1(*b*) shows the response of the variance estimation when a conventional wall filter is used, showing the near binary effect. To obtain the results shown, the simulation process was modified by putting the backscattered pulse through a first-difference FIR filter which attenuated the d.c. component before doing the autocorrelation calculation.

To better image the vibration patterns in deeper tissue a series of new filters were designed and installed on the Logiq 700 scanner. These filters selectively attenuate the d.c. in the power spectrum and thereby increase the importance of the higher spectral components in the variance calculation. Figure 1(*c*) shows the response of the vibration estimator with

a sensitivity-enhancing filter, which attenuates the d.c. component by 20 dB. The filter is monotonic up to the maximum estimate and allows imaging of much lower vibration amplitudes. These results were obtained by modifying the simulation process by putting the backscattered pulse through a first difference FIR filter which retained the desired d.c. component before doing the autocorrelation calculation.

2.2.3. Power Doppler for vibration imaging. Power Doppler is available on many commercial ultrasound scanners and is widely used for flow imaging so it is natural to consider the question of whether power Doppler would be suitable for vibration imaging. According to Rubin *et al* (1995), power Doppler imaging maps the integrated Doppler power spectrum, i.e. the zero lag of the autocorrelation function, to a colour overlay. The detection sequence is otherwise identical to colour flow Doppler up to that point. Babcock *et al* (1996) report that a wall filter is used to reduce signals from vessel walls in power Doppler imaging and that all moving particles yield a colour signal irrespective of their speed or direction. The more particles there are in motion in an imaging cell the stronger (brighter) the colour signal.

Using this description the vibration response of power Doppler was simulated by modifying the computer model so that it performed as described. The results shown in figure 2 plot the vibration amplitude versus power. The figure contains a family of curves, one for each of three signal strengths in the image. It is clear that the power from an imaging cell with strong scatterers will be greater than that from an imaging cell with weak scatterers. Because of this, power Doppler cannot be used to image the relative vibration amplitude between areas with different grey-scale values in the B-scan. It should be pointed out that the variance method of vibration estimation uses the normalized autocorrelation function and hence is very robust in making correct vibration estimates regardless of the echogenicity of the imaging cell.

2.3. Modal theory

Modal patterns can occur when regular geometries and low-loss conditions are present, for example at low frequencies in a liver phantom. Parker and Lerner (1992) reported observing modal patterns in the kidney of a healthy volunteer when vibrated at 100 Hz, the liver of a healthy volunteer at 100 Hz and at higher frequencies and the normal breast at multiple frequencies. These modal patterns, which are standing waves in the vibration field, have been a key source of artefacts in phantom imaging experiments. In this section we analyse these patterns from a mathematical perspective and present a strategy on how they might be reduced. Figure 3 shows co-registered sonoelastography images of a spherical tumour in a bowl-shaped liver phantom taken at different vibration frequencies illustrating the imaging problem that modal patterns in the vibration field cause for differentiating hard and soft tissue. The modal patterns for each frequency are clearly visible as alternating bands areas of bright green and dark green. Modes naturally arise from the governing elastodynamic equations when a wave is confined in a bounded region of space. The modal pattern is a spatial characteristic function or eigenfunction that satisfies the governing differential equations and the associated boundary conditions at a specific frequency (the eigenfrequency). Although modal patterns represent actual tissue vibrations, they are undoubtedly artefacts when the objective is detection of a tumour.

Solutions to the natural vibration of an elastic solid of finite extent are extremely difficult to obtain analytically except for certain highly regular shapes such as a sphere and a rectangular solid. In practice numerical methods including finite elements and finite difference are used to obtain solutions for more arbitrary shapes. These methods provide less insight into the processes occurring so we choose to illustrate our method for reducing modal artefacts

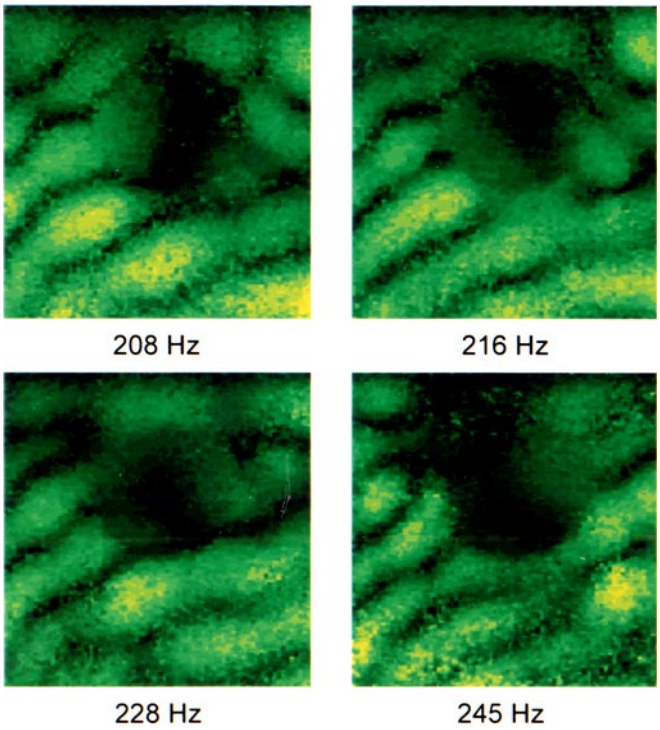

Figure 3. Sonoelastography images of a bowl-shaped tissue phantom containing a spherical tumour taken at four different vibration frequencies to illustrate the modal pattern effect. The region displayed is 4 cm by 4 cm and the tumour diameter is 1.5 cm. The image plane is parallel to the direction of the applied vibration.

by obtaining the eigenmodes of a rectangular elastic solid with fixed boundary conditions. A sketch of the solid is shown in figure 4. The governing equations are:

$$\vec{\mu} = \nabla\Phi + \nabla \times \vec{\Psi} \tag{8}$$

$$\nabla^2\vec{\Psi} = \frac{1}{c_T}\frac{\partial^2\vec{\Psi}}{\partial t^2} \tag{9}$$

where $\vec{\mu}$ is the displacement vector, Φ is the scalar potential function for the acoustic wave, $\vec{\Psi}$ is the vector potential function for the shear waves and c_T is the shear (transverse) velocity. The acoustic wavelength of longitudinal compression waves at 600 Hz is about 2.5 m so we need not concern ourselves with acoustic modes for small organs at low frequencies. The equation for the displacement field then simplifies to

$$\vec{\mu} = \nabla \times \vec{\Psi} \tag{10}$$

which expressed in component form is

$$\begin{aligned}
\mu_x &= +\frac{\partial\Psi_z}{\partial y} - \frac{\partial\Psi_y}{\partial z} \\
\mu_y &= -\frac{\partial\Psi_z}{\partial x} + \frac{\partial\Psi_x}{\partial z} \\
\mu_z &= +\frac{\partial\Psi_y}{\partial x} - \frac{\partial\Psi_x}{\partial y}.
\end{aligned} \tag{11}$$

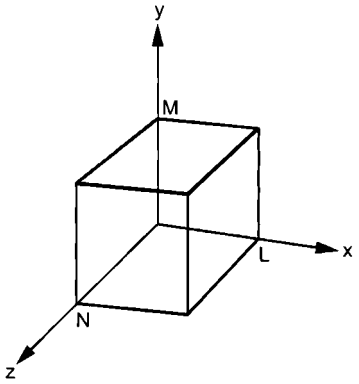

Figure 4. Coordinate system and boundaries of the rectangular elastic solid with sides L, M, N in the x, y and z directions respectively.

Since we will be considering only forced sinusoidal vibration, the vector wave equation in (5) reduces to the vector Helmholtz equation which, expressed in component form, is

$$\begin{aligned} \nabla^2\Psi_x &= -k^2\Psi_x \\ \nabla^2\Psi_y &= -k^2\Psi_y \\ \nabla^2\Psi_z &= -k^2\Psi_z \end{aligned} \tag{12}$$

where $k^2 = \omega^2/c_T^2$ and ω is the radian frequency of the vibration. The fixed boundary conditions ensure that the normal displacement at each of the fixed surfaces is zero, which gives us six boundary condition equations, which are

$$\begin{aligned} \mu_x|_{x=0} &= 0 \qquad & \mu_x|_{x=L} &= 0 \\ \mu_y|_{y=0} &= 0 \qquad & \mu_y|_{y=M} &= 0 \\ \mu_z|_{z=0} &= 0 \qquad & \mu_z|_{z=N} &= 0. \end{aligned} \tag{13}$$

Using the above equations it is straightforward to verify that a solution for the vector potential function is

$$\Psi_x = \Psi_y = \Psi_z = \sin(l\pi x/L)\sin(m\pi y/M)\sin(n\pi z/N) \tag{14}$$

where l, m and n are integers. The set of natural frequencies is derived by substituting the relation for k and solving for the frequency

$$f_{lmn} = \frac{c_T}{2}\left(\frac{l^2}{L^2} + \frac{m^2}{M^2} + \frac{n^2}{N^2}\right)^{1/2}. \tag{15}$$

The values of f_{lmn}, the natural frequencies, are discrete and form an infinite set.

When forced vibration is applied to an elastic solid which has no damping, the solution takes on two forms. If the applied vibration frequency is not a natural frequency many of the eigenmodes with natural frequencies near the applied frequency are excited and the vibration field tends to be uniform. If the applied vibration is a natural frequency, resonance occurs and the spatial vibration pattern for that mode predominates in the vibration field, producing the undesirable modal artefact. Given the fact that real elastic solids have damping, the resonance at the natural frequency has a Q factor. So vibration at or near a natural frequency excites the eigenmode for that frequency and eigenmodes which are close (within the 3 dB bandwidth defined by the Q factor) to the applied frequency are excited. This forms the basis of a strategy

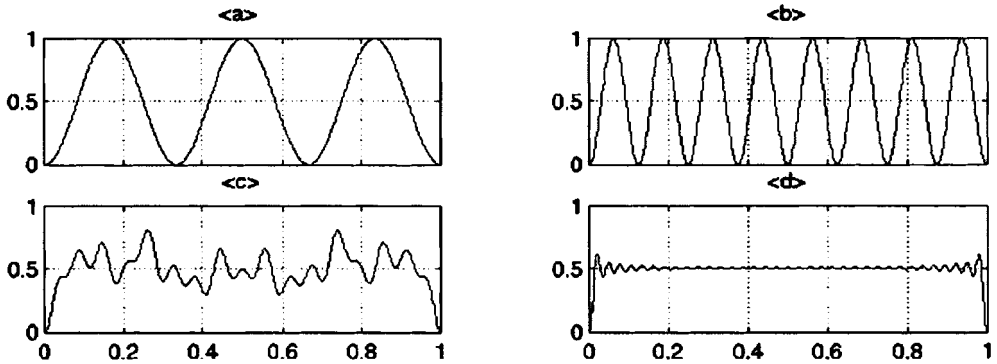

Figure 5. Eigenmodes of the square of the peak vibration are shown since the variance estimator is linear in that variable: (*a*) and (*b*) plot a typical eigenmode for the rectangular solid; (*c*) an average of 6 eigenmodes and (*d*) an average of 35 eigenmodes.

used for eliminating modal pattern artefacts. A chord of multiple harmonic tones applied to the tissue will produce a resulting vibration pattern that is more uniform than that seen in pure tone forced vibration. The use of harmonic tones is required by the fact the variance estimator is most accurate when the sampling window corresponds to an integer number of periods of the applied vibration.

Figure 5 shows, in one dimension, two representative vibration eigenmodes, along with the two averages of several frequencies. Averaging any set of eigenmodes will result in a smoother vibration pattern. Stated formally, using variance as a metric for smoothness, the variance of the function $|\sin(nx)|$ for any integer value of n is identical, and the variance of the average of M such functions will be the original variance divided by M. Simply stated, the strategy to obtain a uniform vibration pattern is to excite as many modes as possible. In real-time this would be implemented by using a polychromatic signal to drive the shear wave source. Each tone would excite the mode(s) whose eigenfrequency is close to its frequency, resulting in a vibration pattern (for a homogeneous region) more uniform than that of each individual tone. In our experimental technique the objective was to set the relative voltages between each chord so the each tone would have equal spectral variance, as seen by the variance estimator.

2.4. Vibration source—transducer with piston applicator

A vibration shaker purchased from Vibration Test Systems (VTS, Aurora, Ohio) provided the low-frequency acoustic field for the phantom and *ex vivo* experiments. The shaker was driven by an amplifier whose voltage output could be precisely controlled by a frequency generator and was provided with an applicator attached to a metal rod which is vibrated like a piston, transferring the low-frequency acoustical vibrations to the phantom. The shaker (model # VTS-100) is rated as having a peak vibration amplitude of 279 μm at 300 Hz and 152 μm at 400 Hz when driving a load of 154 g. Before imaging, the tissue sample was brought into solid contact with the applicator to ensure an efficient transfer of vibration to the phantom.

2.5. Prostate phantom

An ultrasonic tissue mimicking prostate phantom was purchased from Computer Imaging Reference Systems (CIRS, Norfolk, Virginia) to test the imaging system. An ellipsoidal tumour, whose largest axis was 11 mm, was embedded by the manufacturer in the left lobe

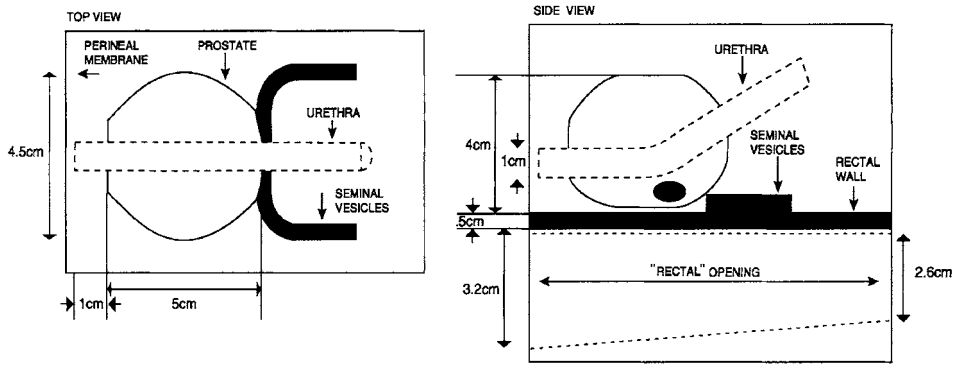

Figure 6. Schematic diagram showing top and side views of the prostate phantom. The soft Zerdine phantom is enclosed in a clear casing shown as the boundary of the sketch. The black ellipse shows the location of the hard tumour near the base of the gland. (©1999 Computer Imaging Reference Systems, used with permission.)

of the gland near the base. The tumour was colour coded with a reddish dye and was visibly distinct from the rest of the gland, which was dyed light blue. However, the tumour was specified to be isoechoic when viewed in B-mode. The tumour material was made of the same chemical compound as the surrounding tissue, except the amount of cross-linking was modified to increase the Young's modulus. Static elasticity measurements made of material samples provided by the manufacturer revealed that the tumour had an elasticity seven times greater than the surrounding tissue in the prostate. Figure 6 shows the manufacturer's schematic diagram of the phantom.

The phantom was imaged using ultrasound. 2D and 3D standard grey-scale and vibration images were acquired. The phantom was also imaged using magnetic resonance imaging (MRI) and 2D MR slices were acquired at 2.5 mm intervals. The 2D ultrasound data were acquired at 1 mm intervals. After it was noted that the tumour was visible and distinct in the MR images, the MRI was used as the gold standard to judge the accuracy of the rendering of the tumour in sonoelastography.

2.6. Image processing

The GE Logiq 700 ultrasound scanner that was used came equipped with the Extend research package and the modifications required for sonoelastography imaging. This included special colour maps in the colour flow Doppler mode which mapped only the variance of the power spectrum to the screen, the special filters for vibration imaging sensitivity enhancement and the ability to save the screen images to a hard drive in the machine in PNM format. This image storage capability allowed the capture of both still frame and cine-loop sequences of co-registered B-scan and variance (vibration) images. The cine-loop mode was used in conjunction with a linear track-stepper motor assembly to capture sequential tomographic slices for three-dimensional imaging. By attaching and aligning the ultrasound transducer to the linear track so that the image plane was perpendicular to the allowable direction of motion, all images acquired were parallel. The velocity of the stepper motor was synchronized with the scanner's frame rate so that images were acquired at a known spatial interval.

After file acquisition the files were transferred using FTP to a computer workstation in the department's image processing laboratory where they were converted to Sun raster or tiff format and cropped for viewing. The vibration images, which are 4 bit/16 level grey-scale images were

most often viewed on a green-scale pseudo-colour map to enhance contrast and visualization of tumours. For the 3D images, the converted and cropped Sun raster cine-loop sequences were assembled into a volume using C++ software developed in-house. The 3D image format was designed to be compatible with the SGI Explorer software used for visualization. The segmentation of the 3D images was performed using a statistical test employing local mean and variance information (Tamez-Pena 1999). This 3D segmentation techniques uses a $3 \times 3 \times 3$ voxel mask to calculate the local mean and variance of each voxel in the image. Each voxel is then assigned to a segmentation object based on how close those two parameters are to its neighbours in a parameter space. The compactness of the resulting segmented object is also taken into consideration.

2.7. Ex vivo prostate

An excised prostate obtained from a patient undergoing radical prostatectomy as treatment for prostate cancer was imaged immediately after excision then passed on to pathology for histological examination. The sample was placed in a specimen holder which consisted of a hollow Plexiglas cylinder (9 cm inside diameter) with both ends open. The bottom of the cylinder was covered with a thin plastic film (Saran Wrap) and secured with a rubber band to ensure that the contents would not leak. A 2 cm thick, 9 cm diameter stand-off pad was placed in the bottom of the cylinder after a shallow depression was carved out of the top of the pad to cradle the prostate specimen. The prostate was then placed on top of the stand-off pad. Additional stand-off pads, whose centres had been cut out to form rings, were then placed in the cylinder, surrounding, but not touching the prostate so that the top-most pad was near the top of the specimen. Once placed in the stand-off pad nest, the prostate specimen was surrounded with acoustic gel to provide a path for the ultrasound. The prostate was oriented so that the rectal surface was posterior facing the applicator surface of the vibration piston. The piston-shaped applicator with a 2.5 cm diameter was brought in contact with the bottom of the specimen holder so that it could transfer vibration to the gel pad. The vibration source described in section 2.4 was used to provide vibration.

The volume was scanned axially on the anterior surface from the apex to the base of the prostate. The scan was accomplished with a linear probe (a 739L) on the GE Logiq 700 scanner at 5 MHz Doppler frequency. The probe was mechanically translated in 1 mm increments along a linear track until the whole volume of interest was imaged using the single-frame capture capabilities of the Extend research package. The image slices were stacked up like a deck of cards to create a three-dimensional image. 306 Hz was selected as being high enough to provide good vibration contrast between tumour and normal tissue while still being low enough to make it possible to induce vibration at amplitudes that could be detected. A frequency generator was used to provide the pure tone vibration. A polychromatic vibration source was not available at the time the gland was excised. The vibration was in the vertical direction and all images were acquired in the vertical plane parallel to it.

3. Results

3.1. Prostate phantom: comparison of MRI and sonoelastography

Figure 7 shows co-registered 2D images of the phantom using MRI, B-scan imaging and sonoelastography. Results of the segmentation of these images are also shown. MR images were acquired every 2.5 mm and ultrasound images were acquired every 1 mm. The images shown are comparable slices where the image plane passes through the tumour. Although MRI

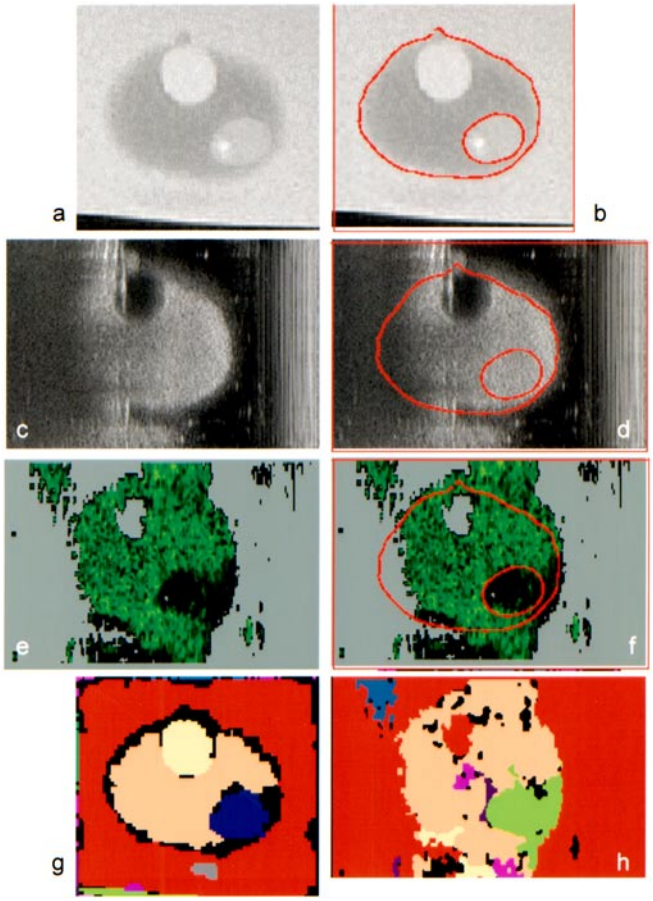

Figure 7. 2D MRI and ultrasound cross-sectional images of the phantom shown in figure 6 in a region containing the tumour. (*a*) MR image: the gland is visible as the darker grey tone against the brighter background. The bright, nearly circular region, anterior in the image, is the urethra and the light grey ellipse, posterior and right in the image, is the tumour. (*b*) Same image as in (*a*) but the gland surface and tumour boundary are outlined in red. (*c*) B-scan image of the phantom at approximately the same image plane as the MR image in (*a*). The scanning transducer was located on the right of the image during acquisition. The outline of the gland is visible but the edge of the gland distal to the transducer is blurred. The urethra is quite visible as a black circular region. (*d*) Same image as (*c*) except the red lines outlining the MR image were overlaid to verify that the regions of interest imaged are comparable. Note that the outline of the tumour from the MR image is located over an isoechoic region of B-scan. (*e*) Sonoelastography image of the same region of interest taken while vibrating at 296 Hz. The bright green indicates areas of high vibration and the dark green areas of low vibration. The urethra is visible as an area of no vibration. (*f*) Sonoelastography image with boundaries from the MR image added. The MR tumour outline aligns well with the area of low vibration in the image except for the dark region that spreads out near the right edge of the gland. The colour Doppler signal shows considerable blooming beyond the true edge of the gland, especially in the lateral direction of the scanning beam (up and down in the image). (*g*) Segmentation of the MR grey-scale image. The tumour is segmented as purple in the image, the urethra is yellow. (*h*) Segmentation of the sonoelastography image. The tumour is segmented as lime green, the urethra as the background orange brown.

does not image elasticity directly, the tumour is visible because of the difference in the cross-linking and its effect on the T_1 and proton density of the material. Using the MR image as the gold standard we note that the area in the MR image showing the tumour location (figure 7(*a*))

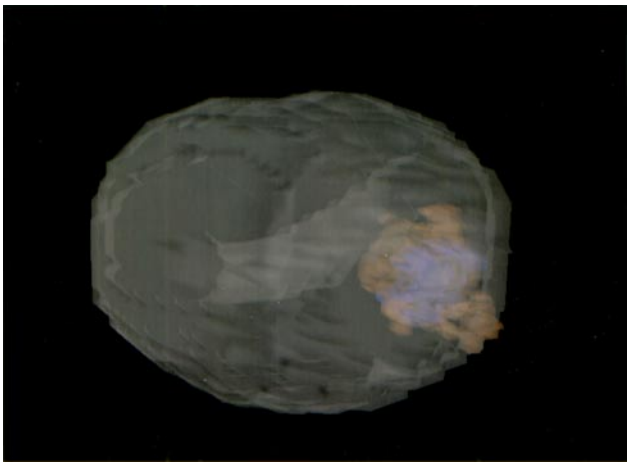

Figure 8. 3D rendering of MR and ultrasound data from the prostate phantom. The MR segmentation of the gland is shown as a surface rendering in transparent grey to serve as a geometrical reference for the tumour. The MR segmentation of the tumour is shown in blue, the segmented tumour from the sonoelastography image is orange. The urethra is visible as a transparent tube running from the apex to the base of the gland.

corresponds fairly well to the area of low vibration in the sonoelastography image (figure 7(*f*)) except where the dark area (low vibration) bleeds towards the gland boundary. It is not clear at this point if this is due to reverberations of the shear waves off the hard plastic container holding the phantom. In figure 7(*f*) the bleeding of the high vibration (bright green) transversely (up and down) beyond the tissue boundary is an artefact most likely to be attributed to excessive gain in the colour Doppler channel.

Some physicians assert that the correct estimation of the tumour volume in prostate cancer *in vivo* would be helpful in formulating treatment for the disease, since (*ex vivo*) determination of tumour volume has been shown to correlate with progression of the disease after radical prostatectomy (Egevad *et al* 1998). The suitability of this imaging technique to estimate tumour volume was evaluated using the tissue phantom. After applying the segmentation technique described in the section on image processing, the tumour volume was estimated by counting the number of voxels in the segmentation. The volume of the segmented tumour in the 3D sonoelastography image was estimated at 0.7 cm^3. When these segmentation techniques were applied to the MRI data set the tumour volume was estimated to be 0.8 cm^3, making the sonoelastography estimate about 88% of the MRI tumour volume. This result should be considered preliminary because of the expected sources of error, such as would result from the different sampling rates chosen for each modality and the bleeding artefact in the US image. Figure 8 shows both the MR tumour (blue) and the US tumour (orange) rendered within the gland. The surface of the gland is rendered as grey and transparent. There is disagreement between the US and MR images in both the image plane (x, y) and axial (z) directions. The MR renders the tumour as larger in the axial direction because of the 2.5 mm distance between slices used during acquisition. The US was acquired in 1 mm slices. The US renders the tumour as larger in the image plane, probably from the bleeding beyond the tumour boundary and blooming of the image beyond the gland boundary visible in the 2D images. Edge definition in sonoelastography requires consideration of a number of factors. Since the vibration field is a continuous function of position and since displacement across the tumour boundary must be continuous there must be some undetermined rate at which vibration amplitude falls off at the

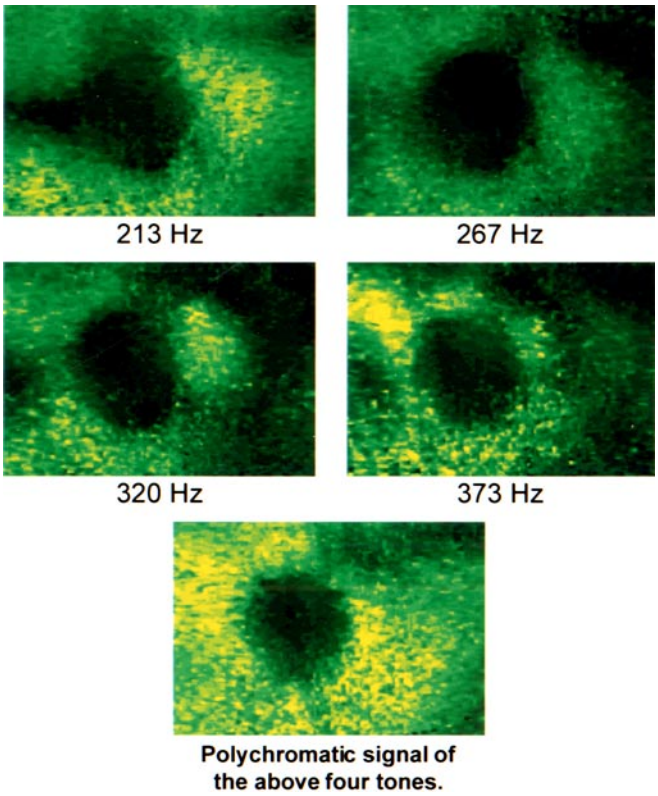

Figure 9. Four co-registered sonoelastography images of a 1.5 cm spherical tumour in a bowl-shaped phantom. The top four images were taken at four different vibration frequencies, the lower image was taken using a polychromatic signal consisting of 213, 267, 320 and 373 Hz. The image plane was normal to the direction of the applied vibration.

transition. The key issue is the distance into the tumour at which the reduced local vibration is achieved, compared with the voxel size of the Doppler estimator.

3.2. Reduction of modal patterns

As discussed in section 2, it is believed that modal patterns can be a key factor limiting accurate rendering of the boundaries of tumours in sonoelastography when using monochromatic excitation in a simply shaped organ. One solution for reduction of these artefacts is the use of polychromatic excitation of the shear wave source. Figure 9 shows four images of a spherical tumour in a phantom taken with the external vibration source driven at four different frequencies. Figure 9 also shows the same region of interest imaged using polychromatic excitation. The tones used for polychromatic excitation were 213, 267, 320 and 373 Hz. These frequencies were used because their fundamental period coincided with the length of a 15-pulse packet using a pulse repetition frequency of 800 Hz. The samples taken for the autocorrelation estimate will then span one period of the applied vibration. The relative voltage amplitudes in the chord were approximately equal to the square of the ratio of the frequency to the lowest tone. This image demonstrates the ability to reduce effects of modal patterns, while maintaining lesion contrast.

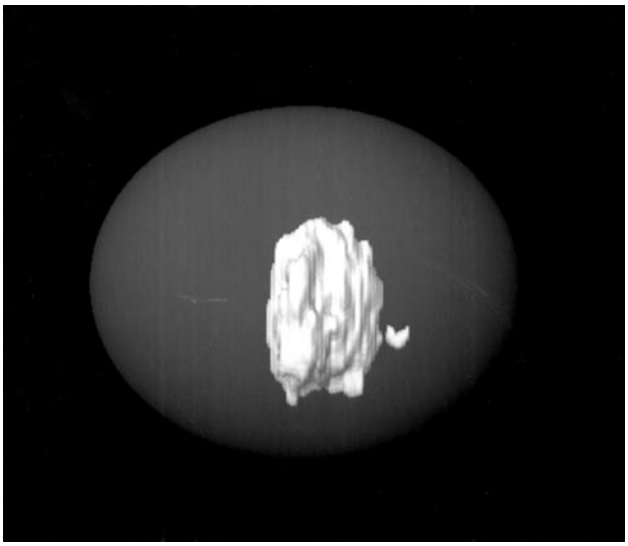

Figure 10. 3D rendering of the sonoelastography data from the *ex vivo* prostate scan seen from the viewpoint of the right side of the patient. The areas of low vibration in the data set have been segmented and rendered as a solid bright grey mass. An ellipse approximating the surface of the gland has been rendered as a transparent grey surface to provide a 3D marker for the tumour. The apex of the gland is on the right and the base on the left in this 3D view.

3.3. Ex vivo prostate study

Figure 10 shows a 3D sonoelastography image of an *ex vivo* prostate taken at a vibration frequency of 306 Hz. The specimen was from a patient diagnosed with prostate cancer and was imaged immediately following excision. In this image the area of low vibration has been rendered as a bright grey mass and the approximate location of the surface boundary of the prostate has been represented as a transparent ellipsoid. After imaging, the gland was examined by pathologists who confirmed the presence of a hard cancer in the mid-gland region of the left lobe, where the hard mass was imaged in the sonoelastogram. They further indicated that there was no cancer in the region showing high vibration (soft tissue) in the 3D rendering.

The pathology report describing the examination of the gland stated the following: the prostate measured 47 mm in the anterior–posterior direction, 55 mm in width (patient's right to left) and 36 mm from apex to base. The gland was fixed in formalin then serially sectioned from apex to base into five regions labelled A to E. The sectioning revealed a 23 mm (anterior to posterior) by 18 mm (patient's right to left) by 18 mm (apex to base) tan-white lobulated nodule with ill-defined borders involving sections A to C in the (patient's) left lobe of the gland.

In the B-scan of this prostate the maximum observed dimensions were 47 mm (anterior to posterior) direction and 36 mm (apex to base). The linear array used was 39 mm long limiting our measurement of the maximum in the right–left direction. Examining the sonoelastograms for the areas where a deficit in vibration is observed we find a connected region with maximum dimensions of 26 mm (anterior to posterior) by 20 mm (patient's right to left) by 22 mm (apex to base) centred in the left lobe of the gland. The ultrasound slices were imaged at 1 mm intervals in the apex to base direction so the slices equivalent to sections A to C defined in the pathology report would be A = {1–7}, B = {8–15}, C = {16–22}. The deficit in vibration

was observed in slices 6 through 27 which traverses sections A through C and about half of section D = {23–29}. If we consider the maximum dimensions of the lesion given in the pathology report and measured in the sonoelastogram as the three axes of an ellipsoid, an approximate volume can be determined and the accuracy of the ultrasound compared with the size determined by pathology. The volume computed by this method from the measurements in the pathology report is 3.9 cm^3 while the volume from the ultrasound measurement is 6.0 cm^3. The measurements from the 3D sonoelastography overestimated the volume by about 50%.

4. Discussion and conclusions

We have demonstrated some principles and practices that underlie the use of real-time vibration sonoelastography. The issues of signal processing and modal patterns are examined and manipulated to optimize the detection of hard tumours. Results from a phantom experiment show that sonoelastography and MR images of the same isoechoic hard lesion agree, except that the sonoelastography rendering of the tumour extended beyond the tumour boundary as determined from the MR image. We hypothesize that this 'blooming' effect was caused by the physical geometry of the phantom and by the extended disturbance created by the hard region. We have also presented a method for minimizing modal artefacts in real-time, and this approach was verified in real-time ultrasound imaging experiments.

Preliminary results of the application of this technique to an *ex vivo* prostate containing cancerous tissue were presented. Segmentation techniques were applied in order to obtain a 3D rendering of the tumour, which was displayed within the approximate surface of the gland to provide a geometric reference. Comparison of the histological delineation of the tumour and the sonoelastography images agreed as to the location of the cancerous tissue.

As sonoelastography is a work-in-progress it is worthwhile to mention some of the open issues involved in this technique. This would include artefacts from vibration source beam patterns which need to be analysed in future work. Diffraction effects have the potential of concentrating the beam energy even when the underlying tissue elasticity is uniform. The impact of the angle between the image acquisition plane and the direction of the forcing vibration also needs to be evaluated. An analysis of the edge sharpness between stiff and normal regions near the tumour would provide insight into the potential accuracy of volume estimation using vibration imaging techniques by answering the question of how localized is the vibration amplitude change at the boundary between a region of lower elasticity and a region with high elasticity. Although these theoretical issues remain, the technology for 3D sonoelastography and understanding of basic principles has now progressed to the point where real-time *in vivo* imaging is possible.

Acknowledgments

This work was supported in part by the NSF/NYS Center for Electronic Imaging Systems, NIH grant 2 R01 AG16317-01A1, the University of Rochester Departments of Radiology and Electrical and Computer Engineering and the General Electric Company (GE). The authors thank GE Medical Systems Division for the loan of the Logiq 700 ultrasound scanner used in the imaging experiments and gratefully acknowledge the insights and assistance received from Drs Anne Hall and Kai Thomenius of GE on a range of topics. Thanks also go to Heather Miller of CIRS for her work in the phantom tumour design and her cooperation in providing material samples for elasticity measurements.

References

Babcock D S, Patriquin H, LaFortune M and Dauzat M 1996 Power Doppler sonography: basic principles and clinical applications in children *Pediatr. Radiol.* **26** 109–15

Carvalhal G F, Smith D S, Mager D E, Ramos C and Catalona W J 1999 Digital rectal examination for detecting prostate cancer at prostate specific antigen levels of 4 ng/ml of less *J. Urol.* **161** 835–9

Catheline S, Wu F and Fink M 1999 A solution to diffraction biases in sonoelasticity: the acoustic impulse technique *J. Acoust. Soc. Am.* **105** 2941–50

Egevad L, Norberg M, Mattson S, Norlen B J and Busch C 1998 Estimation of prostate cancer volume by multiple core biopsies before radical prostatectomy *Urology* **52** 653–8

Ellis J H, Tempany C, Sarin M S, Gatsonis C, Rifkin M D and McNeil B J 1994 MR imaging and sonography of early prostatic cancer: pathologic and imaging features that influence identification and diagnosis *AJR Am. J. Roentgenol.* **162** 865–72

Gao L, Alam S K, Lerner R M and Parker K J 1995 Sonoelasticity imaging: theory and experimental verification *J. Acoust. Soc. Am.* **97** 3875–86

Gao L, Parker K J, Lerner R M and Levinson S F 1996 Imaging of the elastic properties of tissue—a review *Ultrasound Med. Biol.* **22** 959–77

Huang S R, Lerner R M and Parker K J 1990 On estimating the amplitude of harmonic vibrations from the Doppler spectrum of reflected signals *J. Acoust. Soc. Am.* **88** 310–17

Jensen J A 1996 *Estimation of Blood Velocities Using Ultrasound* (New York: Cambridge University Press)

Kasai C, Namkawa K, Koyano A and Omoto R 1985 Real-time two dimensional blood flow imaging using an autocorrelation technique *IEEE Trans. Sonics Ultrason.* **32** 458–64

Krouskop T A, Doughtery D R and Levinson S F 1987 A pulsed Doppler ultrasonics system for making noninvasive measurements of the mechanical properties of soft tissues *J. Rehab. Res. Biol.* **14** 1–8

Lerner R M, Parker K J, Holen J, Gramiak R and Waag R C 1988 Sono-elasticity: medical elasticity images derived from ultrasound signals in mechanically vibrated targets *Acoustical Imaging, vol 19, Proc. 16th Int. Symp.* (New York: Plenum) pp 317–27

Melchior S W and Brawer M K 1996 Role of transrectal ultrasound and prostate biopsy *J. Clin. Ultrasound* **24** 463–71

Obek C, Louis P, Civantos F and Soloway M S 1999 Comparison of digital rectal examination and biopsy results with the radical prostatectomy specimen *J. Urol.* **161** 494–9

O'Donnell M, Skovorada A R, Shapo B M and Emalianov S Y 1994 Internal displacement and strain imaging using ultrasonic speckle tracking *IEEE Trans. Ultrason. Ferroelectr. Freq. Control* **41** 314–25

Ophir J, Cespedes I, Ponnekanti H, Yazdi Y and Li X 1991 Elastography: a quantitative method for imaging the elasticity of biological tissues *Ultrason. Imaging* **13** 111–34

Parker K J, Fu D, Gracewski S M, Yeung F and Levinson S F 1998 Vibration sonoelastography and the detectability of lesions *Ultrasound Med. Biol.* **24** 1437–47

Parker K J and Lerner R M 1992 Sonoelasticity of organs: shear waves ring a bell *J. Ultrasound Med.* **11** 387–92

Rubin J M, Adler R S, Fowlkes J B, Spartt S, Pallister J E, Chen J F and Carson P L 1995 Fractional moving blood volume: estimation with power Doppler US *Radiology* **197** 183–90

Tamez-Pena J G 1999 Four-dimensional reconstruction and visualization of complex musculoskeletal structures *PhD Thesis* University of Rochester, Rochester, NY

Yamakoshi Y, Sato J and Sato T 1990 Ultrasonic imaging of internal vibrations of soft tissue under forced vibration *IEEE Trans. Ultrason. Ferroelectr. Freq. Control* **37** 45–53